

## Magnetic reversal modes in cylindrical nanowires

This content has been downloaded from IOPscience. Please scroll down to see the full text.

View [the table of contents for this issue](#), or go to the [journal homepage](#) for more

Download details:

IP Address: 129.132.208.101

This content was downloaded on 28/12/2014 at 16:26

Please note that [terms and conditions apply](#).

# Magnetic reversal modes in cylindrical nanowires

Yu P Ivanov<sup>1,2</sup>, M Vázquez<sup>1</sup> and O Chubykalo-Fesenko<sup>1</sup>

<sup>1</sup> Institute of Materials Science of Madrid, CSIC, 28049 Madrid, Spain

<sup>2</sup> Far Eastern Federal University, 8 Sukhanova St., 690950 Vladivostok, Russia

E-mail: [ivanov.yup@gmail.com](mailto:ivanov.yup@gmail.com)

Received 15 June 2013, in final form 24 August 2013

Published 6 November 2013

Online at [stacks.iop.org/JPhysD/46/485001](http://stacks.iop.org/JPhysD/46/485001)

## Abstract

We perform a systematic study based on micromagnetic simulations of the demagnetization process for cylindrical nanowires with different crystalline structure. These simulations correspond to the most commonly reported electrodeposited nanowires, based on permalloy, nickel, iron and cobalt, with crystal structure tailored by electrodeposition parameters. The dependence of coercivity and remanence on the nanowire diameter, the angular dependence of coercivity and the corresponding reversal modes are calculated and discussed. Extensive comparison of the obtained coercive field value with available experimental data is presented. Depending on the crystallographic structure, the nanowires reverse magnetization by transverse or vortex domain walls and can exhibit the vortex structure along the whole nanowire length. The state diagrams for reversal modes in different materials as a function of the exchange correlation length, nanowire diameter and the anisotropy direction are presented. Magnetic force microscopy images corresponding to different structures are also evaluated by the micromagnetic simulations.

(Some figures may appear in colour only in the online journal)

## 1. Introduction

Magnetic nanowires (NWs) with diameters of the order or less than the single domain limit, as well as their arrays, are very attractive for applications in nanoelectronics, chemical and biological sensing or medicine [1–8]. NWs with diameters down to 10–20 nm and high aspect ratios can be prepared using templates, such as nanoporous membranes, which is difficult to achieve by other techniques such as conventional lithographic processes. The most attractive features of this method are cost-effectiveness, simplicity of operation, ability to deposit onto substrates with complex geometries and very high axial NWs aspect ratio. Hexagonal highly ordered anodic alumina oxide (AAO) membranes are usually prepared by the two-step anodization process of high purity aluminum foils [9, 10]. The two steps are performed in sulfuric or oxalic bath acid solutions. Depending on the type of acid, the size of the pores is varied from tens nanometres to hundreds nanometres. The typical pore diameters are of around 20 nm or 35 nm with interpore distance 55 nm or 105 nm [11, 12], respectively, while the NW diameter can be continuously changed using chemical etching. Electrodeposition is not

limited to single-element material (Co, Fe, Ni); but also alloys such as, for example, permalloy FeNi (Py) can be used. The AAO membrane can be dissolved and the properties of individual NWs can be studied [13–16].

Significant progress achieved in this area over the past few years has allowed investigating magnetic properties of arrays consisting of NWs with diameter of several tens of nanometres, perfect cylindrical shape and single-crystallinity along the entire several micrometre length of the NW [14, 17–19]. The exact knowledge about magnetization reversal mechanism is very important in most of the application areas. Analytical theory for magnetization reversal in NWs is closely related to the nucleation problem in magnetic bodies having the form of ellipsoid of revolution [20]. This approach is also possible for infinite cylinders, predicting coherent rotation for small NW radius or magnetization curling mode, if the NW radius is larger than some critical value [21]. More recently, the nucleation theory has undergone several generalizations. For example, Escrig *et al* [22] have generalized the results of Aharoni [21], taking into account localized nucleation in the volume of the order of the exchange correlation length. They have discussed three main reversal modes for isolated

cylindrical NWs, depending on their geometry: coherent rotation, transverse domain wall (TDW) and vortex domain wall (VDW) modes. The coherent mode corresponds to homogeneous rotation of magnetization at unison along the whole length of the NW. The transverse and vortex wall reversal modes correspond to nucleation and propagation of a domain wall-like (transverse or vortex type) in long NWs. The transition between two last modes is expected to occur with the increase of NWs diameter [23].

The nucleation theory has been frequently used to determine the coercivity mechanism in NWs. However, analytical calculations based on the aforementioned approach can only qualitatively describe the experimental results [22, 24, 25]. First of all, the analytical calculations are based on some pre-defined form for the magnetization distribution with trial ansatz functions for non-coherent modes. Secondly, the models simplify or do not consider real geometry, structural characteristics of NWs as well as realistic magnetocrystalline anisotropy (MA) and frequently simplify the magnetostatic energy calculation. To improve the description, Skomski *et al* [26] have proposed the localized reversal mechanism taking into account localized nucleation of DWs in defects originating from polycrystallinity, thickness fluctuations, impurities, or local geometrical features at the wire ends, or from a combination of these factors. These defects are responsible for the reduction of experimental coercivity value when compared with the data deduced from analytical calculations.

Magnetic anisotropy of NWs can include the shape anisotropy (frequently this component is dominating due to the high length/diameter aspect ratio), magnetocrystalline anisotropy, magnetoelastic and surface anisotropy. All anisotropy components can be included in analytical calculations by using the ‘effective’ magnetic anisotropy concept, with the value, fitted to experimental data. For example, the fitting of the experimentally measured angular dependence of coercivity [24, 25] to models based on TDW or curling within finite volume (similar to VDW) has allowed one to associate the coercivity mechanism in Co-based NWs with possible occurrence of these processes.

Micromagnetic simulation is a powerful instrument to investigate the magnetization reversal modes in NWs as well as their ordered arrays [23, 27–31]. These simulations enable the prediction of the reversal mode without any simplifications related to its functional form and magnetostatic fields. Previous dynamic micromagnetic simulations [23, 30, 31] in NWs revealed that the magnetization reversal process normally takes place by the nucleation of domain walls at the ends of a NW and subsequent depinning and propagation along its length. The DW structure is TDW or VDW depending on the NW diameter [30]. In addition, recently we have shown that in NWs with strong uniaxial magnetocrystalline anisotropy the remanent magnetization can be characterized by the vortex-like configuration in a whole NW, depending on the direction of magnetocrystalline easy axis with respect to the NW axis [14]. This vortex-like configuration in the whole magnetic wire has also been reported in simulations of amorphous microwires with circular anisotropy [32]. The quantitative agreement between simulation data and experimental ones

strongly depends on the inclusion of realistic experimental nanostructure and parameters in the model [14, 33, 34].

The knowledge of the coercivity mechanism in connection with the material structure and geometry of NWs and their arrays is important for engineering their magnetic properties in advanced applications. However, available reports on the micromagnetic simulations of the demagnetization in magnetic NWs are limited and are only related to some specific experiments and given anisotropy terms [35–37]. Additionally, due to the fast recent development of nanolithography, most simulations are related to NWs with rectangular cross-section. In this paper, we present a systematic study on the magnetic reversal modes in NWs as a function of material (Co, Ni, Fe and permalloy (Py)), their diameter, the magnetocrystalline anisotropy and the applied field angle, performed by micromagnetic simulation with finite element discretization. We also evaluate magnetic force microscopy (MFM) images.

## 2. Model description

We have used the parallel computing implementation of the MAGPAR finite element micromagnetic package [38] to analyse the reversal mode in electrodeposited magnetic NWs by evaluating the solutions of the Landau–Lifshitz–Gilbert (LLG) equation that describes the dynamics of magnetic moments subject to internal and external magnetic fields. The dynamics was followed until the equilibrium was reached, corresponding to ‘static’ (Hz-range) hysteresis magnetometer measurements. The NWs have been represented as cylinders of  $2\ \mu\text{m}$  fixed length and different diameters from 20 to 100 nm, thus saving a high aspect ratio of NWs and, therefore, exhibiting strong shape anisotropy. They are discretized in a tetrahedral mesh, and the magnetization orientation is computed in each mesh vertex and interpolated inside. The structure, anisotropy and magnetic parameters of NWs, considered in our simulations, are taken from experiment and shown in table 1. One of the most important parameters in the micromagnetic model is the magnetic anisotropy. We have considered the magnetic properties of the most frequently electrodeposited NWs composition reported in literature, see table 1. Note that two typical values for the magnetocrystalline anisotropy constant of fcc Co are reported in the literature (see table 1). The larger value corresponds to a metastable Co phase which can exist for nanoparticles and NWs. For completeness, we have used both values. For the simulation of polycrystalline Co hcp NW and polycrystalline textured Co(100) NW we have considered a random orientation of magnetocrystalline easy axis in each tetrahedral in 3D space and in-plane of the NW diameter, respectively. The orientation of magnetocrystalline easy axes for cubic anisotropy materials is shown in table 1. The average finite element discretization size was chosen between 4 and 6 nm.

The problem of NW interactions is highly non-trivial and the results strongly depend on the reversal mode and applied field direction. While for the coherent rotation mode the effect of interactions should be large, for a vortex-based reversal mode, it should be small, due to the absence of magnetic

**Table 1.** The NW parameters considered in the simulations. The anisotropy direction for cubic anisotropy is characterized by the Euler angles ( $\theta$ ;  $\varphi$ ;  $\psi$ ) (rad), where:  $\theta$  and  $\varphi$  are angles which form the magnetocrystalline anisotropy axes in spherical coordinates with  $x$ - and  $y$ -axes, the  $z$ -axis coincides with the NW axis and  $\psi$  is the third Euler angle.

Material	Crystal structure	$M_s$ (T)	$L_{ex}$ (nm)	Anisotropy type	Easy axis ( $\theta$ ; $\varphi$ ; $\psi$ ) (rad)	$K_a$ (J m $^{-3}$ )
Py(Fe <sub>80</sub> Ni <sub>20</sub> )	polycrystalline	1.0	5.1	—	—	0.0
Ni(1 1 1) [39]	fcc, [1 1 1]  NW axis	0.61	4.8	cubic	[1 1 1], (0.96; 0; 0.61)	$-0.048 \times 10^5$
Fe(1 1 0) [39]	bcc, [1 1 0]  NW axis	2.15	2.1	cubic	[1 1 0], (0; 0; 0)	$0.48 \times 10^5$
Fe(1 0 0) [39]	bcc, [1 0 0]  NW axis	2.15	2.1	cubic	[1 1 0], (0.79; 0; 0)	$0.48 \times 10^5$
Co(1 1 1) [40, 41]	fcc, [1 1 1]  NW axis	1.75	3.3	cubic	[1 1 1], (0.96; 0; 0.61)	$-2.7 \times 10^5$
						$-0.75 \times 10^5$
Co(1 0 0) [42]	hcp, polycrystalline, texture (1 0 0)	1.75	3.3	easy plane, $\perp$ NW axis	random 2D in-plane	$4.5 \times 10^5$
Co-hcp [42]	hcp, polycrystalline	1.75	3.3	easy axis in each grain	random 3D	$4.5 \times 10^5$

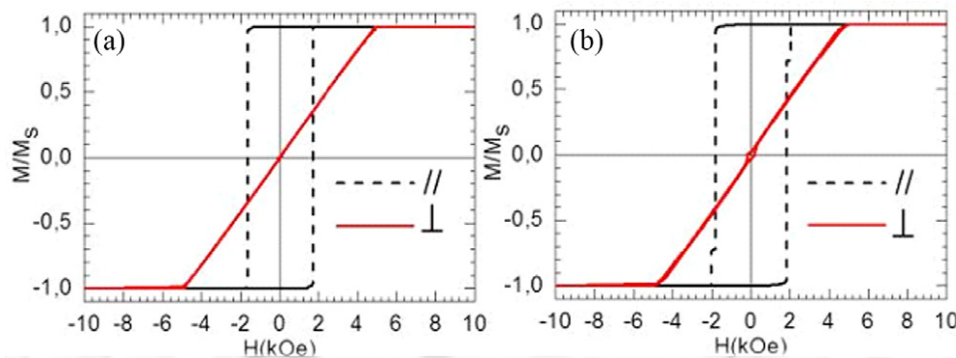


**Figure 1.** The typical hysteresis loops simulated for NWs whose magnetic behaviour is mostly determined by the shape anisotropy. The simulations correspond to a single NW (a), and hexagonal array of 7 Py NWs (b), with 40 nm diameter and 105 nm inter-wire distances.

charges at the NW surfaces. Recently, we have performed the simulation of hexagonal arrays with 7, 19 and 49 Co nanopillars [33]. The value of the coercivity appeared to be only slightly dependent on the number of NWs in array but the perpendicular loops become more sheared, as corresponds to the thin-film geometry. Another effect is that in the larger arrays the magnetization of the whole array is averaged resulting in smoother magnetic loops with the shape closer to experimental one. Since the most important interaction effect is already present in the array of 7 NWs and due to large computational cost for simulating larger array, in this article we restrict ourselves to 7 NWs only with typical parameters for AAO template.

### 3. Magnetic properties of NWs

#### 3.1. Polycrystalline and cubic anisotropy NWs

The magnetization reversal of NWs with polycrystalline structure or with single crystalline cubic anisotropy is mostly determined by the shape anisotropy due to its high value caused by the high aspect ratio length/diameter in comparison with crystalline anisotropy strength. Typical hysteresis loops corresponding to a single and an array of 7 Py NWs are presented in figure 1.

Figure 2 shows the coercivity,  $H_c$ , and the reduced remanence,  $M_r/M_s$ , as a function of the NW diameter in the case of magnetic field applied parallel (||) to the NW axis, simulated for a series of NWs with different

crystalline structure. Very similar coercivity of individual NWs (figure 1(a)) and arrays (figure 1(b)) show that in this particular case the magnetostatic interactions between NWs play a minor role.

For most of these NWs (except Co (1 0 0)) the remanent magnetization practically does not depend on the diameter and the total easy axis is parallel to the NW axis (due to the shape anisotropy). The remanent magnetization structure corresponds to a single domain state. The decrease of the remanence is associated with the formation of an open vortex structure at the NW ends [15] (figure 3(a)). Particularly, one should remember that the formation of such structures, minimizing the magnetostatic energy, does not allow the estimation of the shape anisotropy using simple analytical expressions. In the following, although the micromagnetic simulations calculate the magnetostatic fields exactly, we still phenomenologically use this concept due to its convenience. For polycrystalline textured Co(1 0 0) NW with anisotropy distributed in-plane of NW diameter, the MA starts to compete with the shape anisotropy for diameters larger than 50 nm. This results in the decrease of the remanence. The remanent state in this latter case corresponds to the vortex structure spanning the whole NWs length (figure 3(b)).

For all NWs, the coercivity decreases with the increase of the NW diameter, as corresponds to the decrease of the shape anisotropy which scales with the ratio length/diameter. The value of coercivity depends also on the value of MA (see, for example, curves for Co-hcp and Ni(1 1 1) fcc NWs on figure 2(a)) as well as the orientation of magnetocrystalline



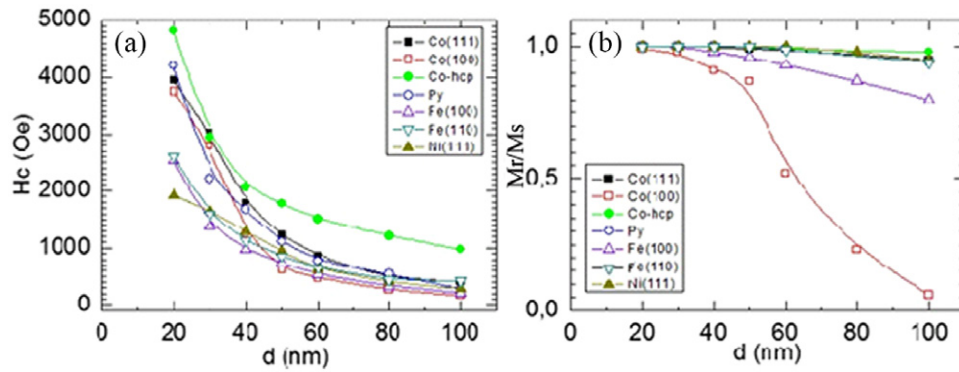


**Figure 2.** The magnetic parameters (coercivity  $H_c$  and the remanence  $M_r/M_s$ ) as a function of the NW diameter for magnetic field applied parallel to the NW axis for a series of polycrystalline and single crystalline NWs with cubic anisotropy.

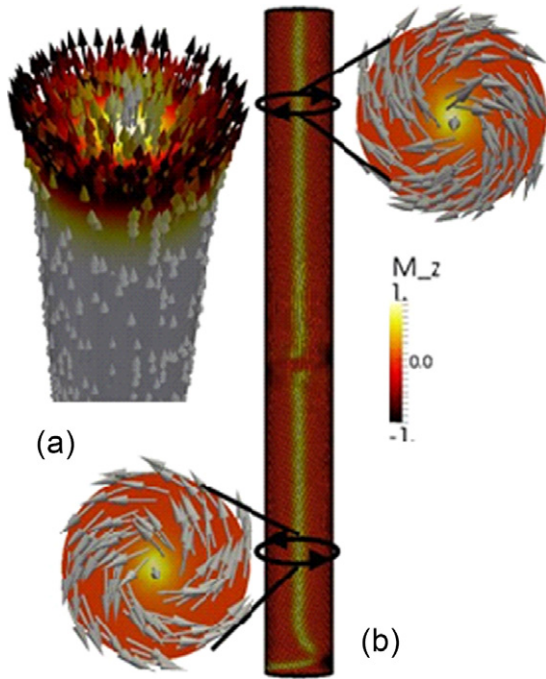


**Figure 3.** (a) The magnetic configuration of the open vortex structure at the NW end (colour corresponds to the component of magnetization parallel to the NW axis, arrows show the magnetization direction). (b) Schematic view of the vortex structure spanning the whole NW's length.

easy axis (see Fe(1 1 0) bcc and Fe(1 0 0) bcc NWs). Note that for the smallest diameters the coercivity of Co and Py NWs is twice larger than for Ni and Fe NWs, which is related to the change of the magnetic reversal mode as will be discussed in section 4. Starting from 50 nm diameter, all NWs (except Co hcp) have similar coercivity. The data represented in figure 2 are in a good agreement with those reported in the literature for NWs with the same geometry and crystal structure (see table 2). Small discrepancies between experimental results and our micromagnetic simulations can be attributed to the change of MA due to the different crystal quality of NWs prepared at different electrodeposition conditions. Also, as shown in figure 2, for Fe NWs with different easy axis orientations and for Co NW with different crystal structures, the coercivity value cannot change too much with the crystal quality of

NWs, especially for NWs diameters larger than 50 nm. Our simulations show that the change of cubic anisotropy in three times, as presented in table 1, does not affect magnetic properties of fcc Co NWs. The data presented in figure 2 can be also applied to the NWs based on Fe, Co, Ni alloys, taking into account that correct simulation parameters can be varied depending on the alloy composition [43, 44] and would change slightly the resulting coercivity value.

Therefore, in the case of Ni and Fe NWs, typically few micrometres in length and tens of nanometres in diameter, the magnetic behaviour is mostly determined by the shape anisotropy ( $\sim 10^6$  erg cm $^{-3}$ ) which overcomes the MA (and magnetoelastic anisotropy) and leads to an easy orientation of the magnetization along the NWs' longitudinal axis [45–58]. The exception is for large diameter NWs formed from the polycrystalline textured Co hcp with random in-plane easy axis.

In the case of magnetic field applied perpendicularly ( $\perp$ ) to the NW axis (parallel to  $x$ -axis) the magnetic behaviour of NWs is practically non-hysteretic (figure 1) and magnetic parameters are almost independent of the NW diameter. Only for Co(1 0 0) textured NW is the coercivity slightly increased for 50 nm diameter.

### 3.2. NWs with competing shape and magnetocrystalline anisotropy (high crystalline anisotropy NWs)

In turn, Co NWs frequently show a preferential, almost single crystal, hcp crystallographic structure [14, 17–19]. The presence of such crystal phase leads to a noticeable uniaxial MA of the same order of magnitude ( $4.8 \times 10^5$  erg cm $^{-3}$ ) as the shape anisotropy. Depending on the orientation of MA easy axis with respect to the NW axis, the MA can both increase and decrease the effective anisotropy of NWs. Consequently, the magnetic properties of Co NWs can be tuned by modifying the crystal growth direction [18, 24] or NWs composition (Co-based alloy NWs) [25].

To study the magnetic properties of Co hcp NWs with competing shape and magnetocrystalline anisotropies, we have considered a single crystal NW with the orientation of MA easy axis ( $c$ -axis) at different angles  $\theta$  with respect to the NW axis. Typical hysteresis loops simulated for NWs with competing shape and magnetocrystalline anisotropies are presented in

**Table 2.** Comparison between simulated coercivity values in various NWs reported in the literature.

Material	$d$ (nm)	Aspect ratio	Length (nm)	$H_c$ (Oe)	
				Simulation	Experiment
Py(Fe <sub>80</sub> Ni <sub>20</sub> )	35	60	2000	1900	1232 [45]
	40–70	80	5000	1620–670	1436–700 [44]
Ni(111)	20	50	1000	1900	970 [46]
	35	60	2000	1350	780 [45]
	30	30	700	1550	1200 [47]
	50	240	12 000	927	624 [22]
	30–100	20	2000	1550–290	1150–300 [48]
	30, 40, 55	20	1000	1620, 1255, 740	1200, 1000, 600 [49]
	180	20	3400	290	215 [50]
Fe(110)	50	1000	50 000	927	1000 [17, 51]
	70	20	1000	555	550 [52]
	20	50	1000	2500	2250 [53, 54]
	80	70	5000	455	450 [55]
Fe(100)	30	170	5000	1700	1720 [55]
	35	120	4000	1245	1250 [56]
Co(111)	20	200	4000	2321	2311 [57]
	40	10	120	1790	1730 [11]
Co(100)	40	130	5000	1790	1760 [58]
	35	120	4000	1900	1848 [59]
	> 100(200, 400)	60	~ 6000	185	175–275 [60, 61]
	30–100	20	2000	2160–185	1490–190 [48]
	40	30	1000	1225	1050 [62], 1250 [63]
	20	500	10 000	3730	3310 [37]
	50	100	5000	680	852 [35]
Co-hcp	90	140	12 000	1112	1100 [16]
	30–100	100	10 000	2950–985	2950–700 [18]
	27, 50	280	14 000	2950, 1720	2620, 1230 [64]
	50	100	5000	1720	1650 [65], 1570 [35]
	30	70	> 2000	2950	3000 [66]

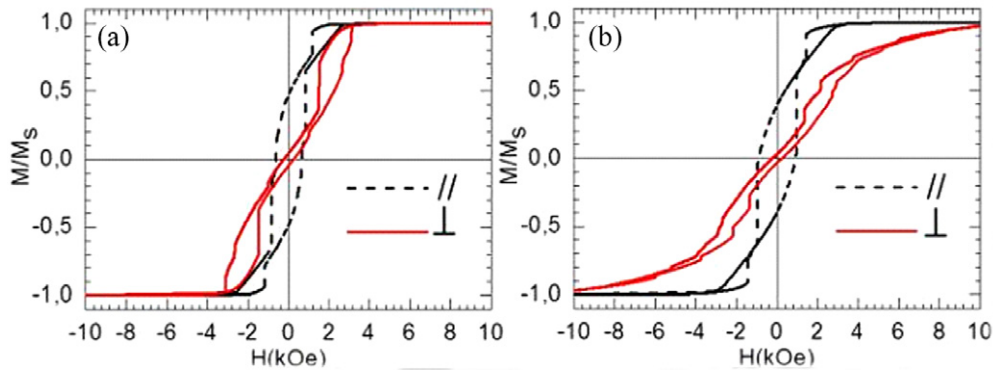
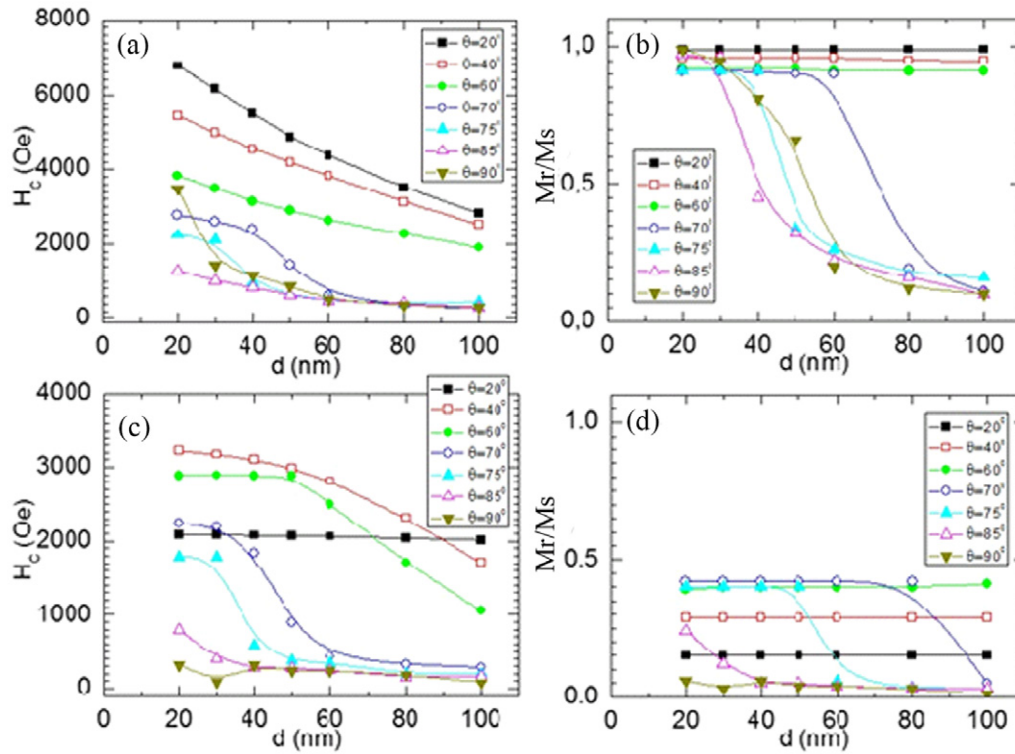
**Figure 4.** The typical magnetic loops simulated for NWs with competing shape and magnetocrystalline anisotropies. The simulations correspond to (a) a single crystal hcp Co NW with  $\theta = 88^\circ$  and (b) hexagonal array of 7 single crystal hcp Co NWs with 40 nm diameter and 105 nm inter-wire distances.

figure 4. More inclined perpendicular loops calculated in the array as compared to individual NWs indicate stronger interactions between NWs in contrast to the case presented in figure 1. As shown in figure 5, the magnetic behaviour of Co hcp NWs strongly depends on  $\theta$  in the interval between  $75^\circ$  and  $90^\circ$ . For  $\theta < 70^\circ$  the MA reinforces the shape anisotropy. When the field is applied parallel to the NW axis, the coercivity is increased as compared with polycrystal NWs (figure 2(a)) and decreases practically linearly with the NW diameter (figures 5(a) and (b)), following the behaviour of the shape anisotropy. At  $\theta > 70^\circ$  the MA tends to compensate the shape anisotropy and both the coercivity and the remanence

decrease drastically with the NW diameter. Note that the critical value of NW diameter at which magnetic parameters start to decrease rapidly is strongly affected by  $\theta$ . The strong decrease of the remanence is associated with the formation of the vortex state along the whole NW length (see figure 3(b), as well as [14] and the next section).

The behaviour of magnetic parameters in the  $\perp$ -field configuration (figures 5(c) and (d)) is also very interesting. When the shape anisotropy is the only anisotropy or when MA easy axis is parallel to the NW axis, the magnetic loops are practically non-hysteretic (similar to those presented in figure 1). For  $0^\circ < \theta < 20^\circ$  the coercivity takes a finite value



**Figure 5.** The magnetic parameters (coercivity  $H_c$  and the remanence  $M_r/M_s$ ) as a function of the NW diameter in the case of magnetic field applied parallel (a)–(b) and perpendicularly (c)–(d) to the NW axis for single crystal Co hcp NWs and different easy axis orientations (defined by the angle  $\theta$  with NW axis).

which does not depend on the NW diameter. The remanence is constant up to  $\theta = 60^\circ$ . With the increase of  $\theta$  the coercivity increases for  $\theta < 40^\circ$  and then it starts to decrease. The critical value of  $\theta$  at which the remanence starts to increase, decreases as a function of the NW diameter. These changes are related to the different reversal modes minimizing the total energy as will be discussed in the next section.

Thus, the orientation of MA easy axis with respect to the NW axis greatly affects the magnetic parameters of high-anisotropy NWs. Several authors [17–19] have reported the experimental data of hcp Co NWs with a good crystallinity (i.e., crystals up to several micrometres in size). The simulation data presented here are in a very good agreement with the experimental ones if the correct orientation of MA easy axis is taken into account [14], see table 2. Therefore, the correct interpretation of experimental data of NWs with strong uniaxial MA requires detailed consideration of their crystal structure.

### 3.3. State diagrams for reversal modes

The analysis of our simulations shows that the reversal modes of NWs with polycrystalline structure or with single crystalline cubic anisotropy correspond to single DW (TDW or VDW) propagation (field applied parallel to NW axis) or quasi-coherent rotation (field applied perpendicularly to NW axis). As before, the exception is the polycrystalline Co(100) NWs with easy plane anisotropy and with diameters larger than 50 nm (see the discussion later). Figure 6(a) shows the state diagram for the DW type as a function of the NW diameter

for different magnetic materials (presented in table 1). The transition from TDW in narrow NW to VDW in NW with the larger diameter only depends on the material, mainly the exchange correlation length [30]. For example, for Fe NWs only VDW is observed, while for Co NWs the transition occurs at 20 nm diameter and for Py NWs at 40 nm.

As shown in figure 2(a) the coercivity for the case of TDW reversal mode is much higher than for VDW mode. In agreement with this, it is well-known that for CoFe-based alloy NWs with several tens of nanometres diameter, the coercivity can be significantly increased by annealing [67–70]. According to our results, this may happen because the saturation magnetization of NWs decreases upon annealing treatment (for example, due to the Fe oxidation or lattice relaxation). As a result, the exchange correlation length is increased and the transition between VDW reversal mode in as-prepared NWs to TDW in NWs after annealing can take place for the same NW geometry, therefore, increasing the coercivity of NW.

Strong uniaxial MA in single crystalline hcp-based NWs significantly affects the magnetic reversal mode. Figure 6(b) shows the diagram of DW type as a function of the NW diameter for Co hcp single crystalline NWs with different easy axis orientations  $\theta$  and in  $\parallel$ -field configuration. The TDW reversal mode is stabilized by MA with easy axis at  $0^\circ \leq \theta \leq 60^\circ$  in the whole range of NW diameters. In  $\perp$ -field configuration the quasi-coherent rotation mode is observed in that case. We call the mode ‘quasi-coherent’ because of some inhomogeneity in the reversal due to different conditions at the NW ends. During the reversal, the spins rotate coherently

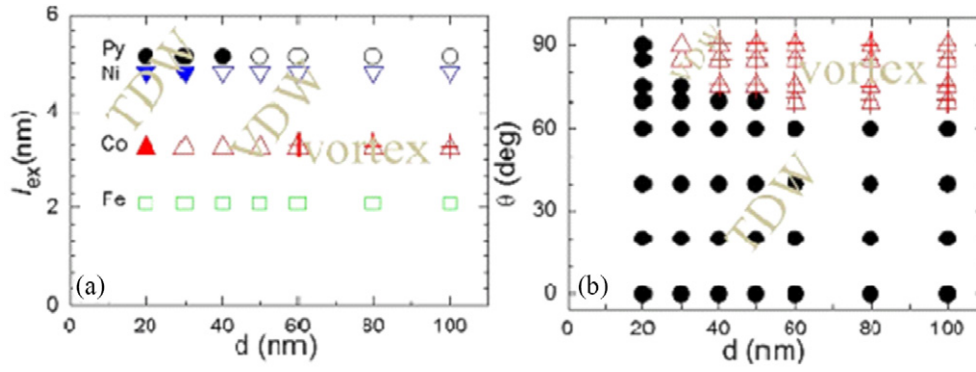


**Figure 6.** The diagram of the DW type in (a) polycrystalline (Co, Py) and single crystalline cubic anisotropy (Co, Fe, Ni) NWs and (b) NWs with single crystalline hcp Co and easy axis direction at the angle  $\theta$  with the NW axis, as a function of the NW diameter. The fill points and open points are TDW and VDW, accordingly. The cross rectangles indicate the area with magnetic vortex state spanning the whole NW length at the remanence and quasi-curling reversal mode for hcp Co NWs polycrystalline (a) and single crystal (b). For fcc Co the state in (a) denoted by crossed triangles remains VDW. The field is applied parallel to NW axis.

**Table 3.** Summary for the reversal mode types in different NW.

Material and NW diameter	Remanent state	Magnetization reversal mode	
		H    NW axis	H $\perp$ NW axis
Py{ $d \leq 40$ nm}, Ni(1 1 1){ $d \leq 30$ nm}, Co(1 1 1), Co(1 0 0), Co-hcp{ $d \leq 20$ nm}, Co( $0 \leq \theta \leq 60$ ) {up to $d = 100$ nm} Co( $\theta = 70$ ) {up to $d = 50$ nm} Co( $\theta = 80$ ) {up to $d = 40$ nm} Co( $\theta = 90$ ) {up to $d = 20$ nm}	Single domain (vortex at the ends)	TDW	Quasi-coherent rotation
Py{ $d \geq 50$ nm}, Ni(1 1 1){ $d \geq 40$ nm}, Co(1 1 1), Co-hcp{ $d \geq 30$ nm}, Co(1 0 0) { $30 \leq d \leq 50$ nm}, Co( $\theta = 90$ ) { $d = 30$ nm}	Single domain (vortex at the ends)	VDW	Quasi-coherent rotation
Co(1 0 0) { $d \geq 60$ nm}, Co( $75 \leq \theta \leq 90$ ) { $d \geq 40$ nm}	Vortex state	Quasi-Curling	Quasi-Curling

inside the NW, with the exception of the spins at the NW ends where the open vortex state is formed at the remanence (see figure 3(a)) and thus the process is different.

For  $70^\circ < \theta < 90^\circ$  there is a transition between the two types walls and the transition diameter decreases significantly with  $\theta$ . Note that for the narrowest NWs (20 nm diameter) the reversal mode is TDW propagation independently on MA easy axis orientation.

Another transition for the reversal mode can be induced by MA with easy axis at  $0^\circ \leq \theta \leq 60^\circ$  for Co NWs with large diameters. Here a quasi-curling reversal mode appears (shown as cross rectangles in figure 6(b)). The same mode occurs for polycrystalline Co(1 0 0) NWs starting with 50 nm diameter (shown as cross rectangles in figure 6(a)). In that case the spins at the remanence form a vortex-like state along the whole NW length (see figure 3(b)) with a core parallel to the initial applied field direction in  $\parallel$  configuration or randomly oriented up/down in  $\perp$  configuration. Due to the high aspect ratio of NWs there are several vortices with alternating chiralities (clockwise/counterclockwise) along NW length. Note that for the  $\perp$  configuration, the number of vortices is larger than for  $\parallel$  configuration. The same transition is also observed for textured Co(1 0 0) hcp NWs with easy plane anisotropy in-plane of NW diameter (see figure 6(a)). We call the corresponding

mode quasi-curling because of different speed of the curling at the NW ends and in the centre. The core of the vortex is remagnetized by domain wall nucleation and propagation.

The summary of different reversal modes is presented in the table 3.

### 3.4. Angular dependence of coercivity

It is common to use the angular dependence of coercivity to analyse the effective anisotropy in NWs and to elucidate the occurrence of different magnetic reversal modes in NWs [56, 57]. For this purpose, the magnetic loops are measured at the different directions of the applied magnetic field with respect to the NW axis (defined by the angle  $\alpha$ ) for hexagonal ordered arrays of NWs [57] or single NW [15]. After that, the data are fitted using the analytical expressions for nucleation field [21, 22]. Specifically, Vivas *et al* [25] basing on analytical models, have concluded about the transition between TDW and VDW modes in CoNi-alloy NWs as a function of the applied field angle.

To clarify the point, we have performed simulation of the angular dependence of the critical fields (nucleation field  $H_n$  and coercivity  $H_c$ ) and the remanence  $M_r/M_s$  for NWs with different reversal modes, based on Py, Fe(1 1 0) and Co (easy axis angle  $\theta = 88^\circ$ ) with 40 nm diameter (figures 7(a)



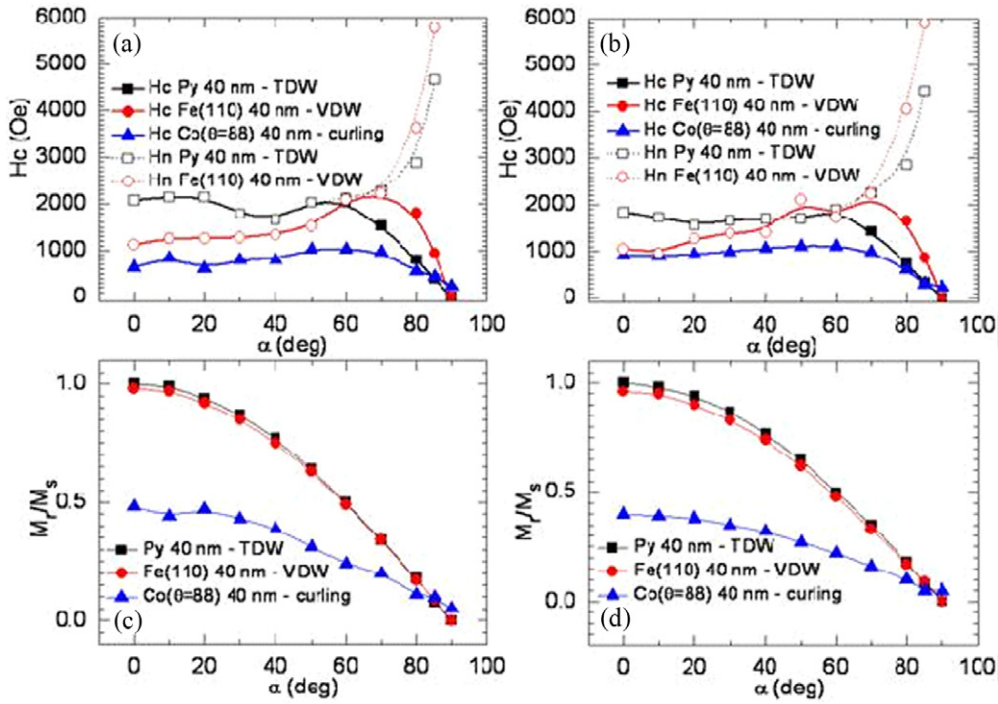


**Figure 7.** The angular dependence of the nucleation  $H_n$  and coercivity  $H_c$  fields (a)–(b) and the remanence  $M_r/M_s$  (c)–(d) for NWs with different reversal modes: (a) and (c) single NWs and (b) and (d)—for hexagonal ordered array of 7 NW with distance between NWs is 105 nm.

and (c)), as well as for hexagonal ordered array of 7 NWs with the centre-to-centre distance between NWs being 105 nm (figures 7(b) and (d)). According to the diagram in figure 6(a), the reversal mode corresponds to the TDW propagation for Py and VDW propagation for Fe(110) and quasi-curling mode for Co NWs, when the field is applied parallel to the NW axis. In our simulations with field applied at different angles, we do not observe the change of the reversal mode type with the applied field angles, except for the exact value  $\alpha = 90^\circ$ , when the TDW or VDW mode is changed to quasi-coherent rotation mode.

We define the nucleation field  $H_n$  as the applied field at which the DW starts to propagate and the coercive field  $H_c$  as the field at which the magnetization is equal zero. As shown in figure 7 the angular dependence of  $H_n$  and  $H_c$  are the same in the range of the applied field angles  $0^\circ \leq \alpha \leq 60^\circ$ . For  $60^\circ \leq \alpha \leq 90^\circ$  the two fields are different: the  $H_n$  starts to increase, while the  $H_c$  decreases. Both angular dependences cannot be described in terms of the Stoner–Wohlfarth model for coherent rotation of magnetization [71]. Aharoni [21] proposed an analytical approach to calculate  $H_n$  for the curling mode. The predicted functional form has the angular dependence similar to that of the nucleation field presented in figure 7, i.e. this value strongly increases as a function of the applied field angle. However, in the case of data in figure 7 the spins reverse progressively via propagation of vortex or transverse DWs. For large applied field angles,  $H_c$  is not equal to  $H_n$  in agreement with the experimental data reported by numerous authors [22, 56, 57].

The angular dependence of  $H_c$  for the curling reversal mode is quite similar: (i) for  $0^\circ \leq \alpha \leq 60^\circ$  the coercivity is

slightly increased with the applied field angles and (ii) starting from  $\alpha = 70^\circ$   $H_c$  starts to decrease. But for TDW and VDW reversal modes the coercivity decreases very rapidly and for  $\alpha = 90^\circ$  the practically unhysteretic behaviour is observed. At the same time for quasi-curling mode the  $H_c$  reduction is much less and the value is not equal to zero for  $\alpha = 90^\circ$  in good agreement with recent experimental data [72]. In contrast, the angular dependences of the remanence for DW reversal modes and for quasi-curling are very different. In the case of TDW and VDW the angular dependence is typical for samples with strong uniaxial anisotropy and is identical for both types of DWs. At the same time, for quasi-curling mode the behaviour is more complex due to the strong competition between MA and shape anisotropy.

As for the comparison between the array and single NW (see figure 7), we practically did not observe too much difference in the functional dependence of  $H_c$  and  $H_n$  on the applied field angle for all types of reversal modes. The magnetostatic interaction between NWs results in a small reduction of the values of  $H_c$  and  $M_r/M_s$  in arrays, as compared to individual NWs.

The analysis of the angular dependence of coercivity presented in several articles [21, 22, 25] is based on the analytical formulae for the nucleation field. Consequently, the functional dependence of coercivity, similar to the one presented in figures 7(a) and (b) has been interpreted as a change of the reversal mode [25]. Our simulations show that the reversal mode remains the same, however, for large applied field angles, the nucleation and the coercivity fields are different. The coercivity field follows the widely observed experimental behaviour while the nucleation field follows its predicted analytical behaviour.

### 3.5. Simulated MFM images of the domain walls structure

A powerful experimental method to investigate the magnetic reversal modes in magnetic nanostructures is the direct observation of the magnetic states by variable-field MFM. The magnetic contrast is recorded as a variation of the magnetic force gradient due to dipolar interaction between the tip magnetization and the stray field emanating from the sample. Due to small dimensions of electrodeposited NWs, the MFM imaging on individual NWs is difficult. However, following further technical developments, several articles have reported recently on the MFM imaging of these objects [13–16, 18, 73].

A powerful method to interpret the MFM imaging is its comparison with the micromagnetic simulations. The MFM images can be easily evaluated from micromagnetic configurations as the divergence of magnetization vector, giving a normally indistinguishable result from the evaluation of the magnetic force derivative. Note that this approach is only valid if (i) the stray field from the NWs is not affected by the tip magnetization and (ii) the stray field from the magnetic tip does not change the magnetic state of NW. The latter can be realized optimizing the experimental conditions (magnetic parameters of the tip, scanning mode, tip-sample distance etc) [18].

The equilibrium magnetic state of most NWs (Py, Ni, Fe, CoFe etc) at the remanence corresponds to almost single domain with magnetization parallel to the NW axis. MFM contrast of such state consists of white and black spots at the ends of NWs from the vortex-like configuration of spins at the ends [15]. Note that at the remanence, these vortices have a so-called ‘open’ structure, i.e. the magnetization in the vortex shell does not lay in-plane but has a non-zero component parallel to the field and responsible for the stray field. Along the NW the MFM contrast should be zero in the ideal case. Such MFM contrast, typical of single domain configuration (i.e., strong contrast at the ends and the lack of contrast at the middle) has been reported by several authors [13, 15, 16, 18].

During the magnetization reversal we have established two types of domain walls: TDW and VDW. The strong magnetic contrast can originate from these DWs pinned at the defects [13]. Both DWs can exist in two types of pairs: the so-called head-to-head and tail-to-tail (see figure 8), depending on the orientation of the magnetization vector in adjacent domains. As shown in figure 8 the contrast from TDW and VDW is quite similar. Note only that TDW contrast is narrower and symmetric with respect to the NW rotation around its axis. Consequently, it will be independent of the NW position with respect to the position on the substrate in the agreement with the experimental results [13, 18]. Differently, the MFM image of VDW is wider and not symmetric with respect to the NW rotation. In its centre the vortex-like structure is present.

A special case corresponds to the magnetic states of NWs with curling-like reversal mode. The equilibrium magnetic state without external magnetic field is the vortex state along the whole NW. Spin configuration consists of several vortices with alternating chiralities (called here chirality-to-chirality walls) and, in the case of  $\perp$  field configuration, also with possibly opposite polarities (called here polarity-to-polarity walls). The MFM contrast from the vortex state should be equal to zero due to the absence of magnetic charges on the

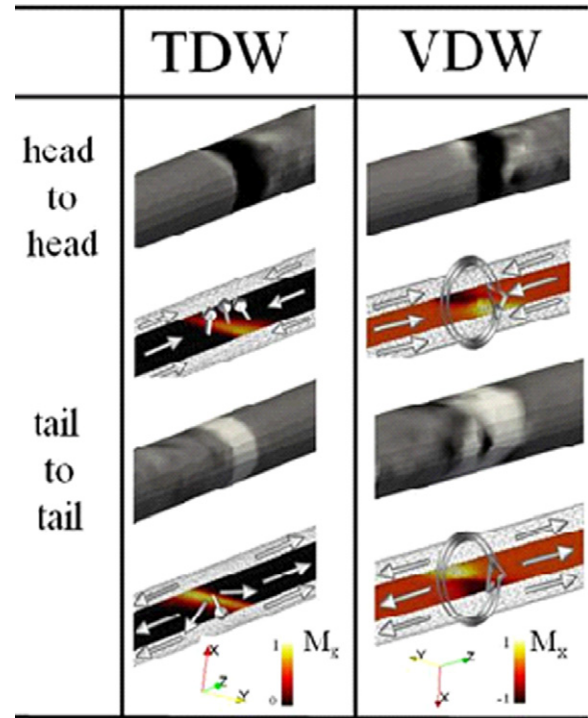


**Figure 8.** The simulated MFM contrast (black and white, upper panels) and spin distribution (coloured, lower panels) in NW cross-section parallel to the NW axis for TDW (Py) and VDW (Fe(110)). The magnetization directions are shown by arrows. The NWs have 40 nm diameter. The MFM contrast for DW was evaluated from transient state during DW propagation at the coercivity field assuming that in the real experiment such contrast appears at the pinning sites along the NW.

lateral surface of the NW (the divergence of magnetization vector is equal to zero), exactly the same as for the single domain state with magnetization parallel to the NW axis. The reason for the appearance of the curling-like structure is the competition of a strong MA anisotropy and the shape anisotropy (figure 6). Depending on the type of MA (uniaxial or easy plane), the magnetization in DWs between vortices is aligned parallel to the easy axis or to the NW axis, as seen in figure 9. Unlike the case of TDW and VDW, MFM contrast from DWs between vortices is different in different cases and is summarized in figure 9, where different contrast is observed for the cases of MA perpendicular and parallel to NW axis as well as for chirality-to-chirality and polarity-to-polarity walls. Note that it is also possible to observe the non-zero MFM contrast from vortices in NWs with a strong MA easy axis directed at  $75^\circ$ – $85^\circ$  with respect to the NW axis. Such an MFM image has been recently experimentally reported for single crystal Co hcp NWs [14].

## 4. Conclusions

By means of micromagnetic simulations, we have systematically studied the magnetization reversal processes in most magnetic nanowires commonly reported in the literature, such as Co, Fe, Ni and Py. Our results allow us to establish a first understanding of the general magnetic behaviour of NWs depending on whether shape anisotropy dominates (soft

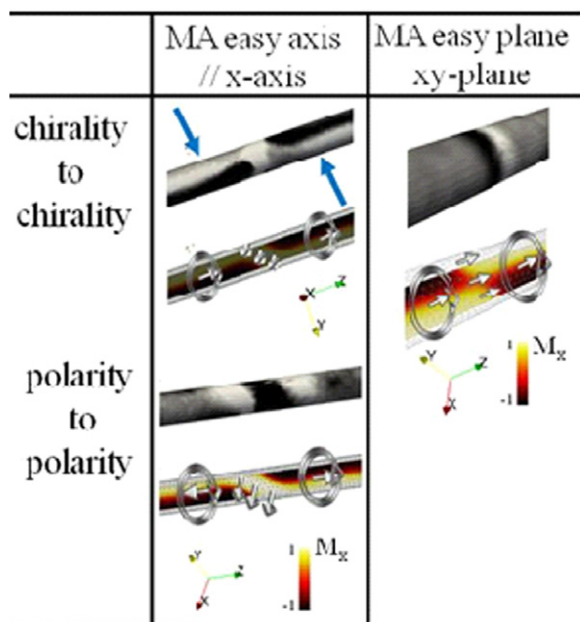


**Figure 9.** The simulated MFM contrast (black and white, upper) and spin distribution (coloured, lower) in NW cross-section parallel to the NW axis in NWs with a vortex magnetic states. The direction of magnetization is shown by arrows.

Fe, Ni, Py and Co nanowires) or there is a competition between shape and magnetocrystalline anisotropy (hard hcp Co-based nanowires) terms. The main results are summarized as the state diagrams for the reversal modes, where the transition between a transverse and the vortex domain wall is represented as a function of the NW diameter.

In most polycrystalline and cubic anisotropy NWs (soft NWs) the remanence is practically constant as a function of their diameter. The reversal mode corresponds to TDW in NWs with small diameters and VDW for NWs with large diameters, the coercivity value being much higher for the TDW than for the VDW. In hard Co-based NWs we report the decrease of the remanence as a function of the diameter, corresponding to the formation of the vortex state along the whole NW. The orientation of the Co hcp easy axis defines the hysteresis process and the corresponding reversal modes undergo the transition between TDW and vortex state along the whole NW as a function of the easy axis angle. The predicted coercivity values are in good agreement with experimental ones reported in the literature, see table 2.

From the analysis of the angular dependence of coercivity in NWs with different reversal modes, our simulations show that for all reversal modes, the angular dependence of coercivity presents a non-monotonic behaviour, i.e. the coercivity field slightly increases for small applied angles and decreases for large angles, in agreement with widely reported experimental results. We did not observe any change of the type of the reversal mode as a function of the applied field angle. The discrepancy with the theory based on the nucleation is explained by the fact that at large applied angles, the coercivity and the nucleation fields are different.

Finally, we have also modelled the MFM images of different domain walls in head-to-head and tail-to-tail

configurations. Our simulations show that the MFM images of TDW and VDW should be similar. In contrast, the NWs with curling-like structure along the whole length (curling-like reversal mode) present different magnetization contrasts, corresponding to chirality-to-chirality or polarity-to-polarity domain walls.

In short, present results constitute a first systematic micromagnetic study of the different coercivity mechanisms in cylindrical nanowires. It is our understanding that it will be particularly useful for the design of advanced applications involving the magnetization reversal of nanowires and specifically based on the use of the vortex state or the motion of magnetic domain walls.

## Acknowledgments

The authors acknowledge the financial support from the Spanish Ministry of Economy and Competitiveness under projects FIS2010-20979-C02-02 and MAT2010-20798-C05-01, from the Regional Government of Madrid under project S2009/MAT-1726, from the European Community's Seventh Framework Program under the project REFREPERMAG, grant agreement 280670, and from the Far Eastern Federal University. Dr Yu P Ivanov wishes to thank the Spanish Ministry of Education for the postdoctoral fellowship during his stay in ICMN/CSIC in Madrid.

## References

- [1] Mourachkine A, Yazyev O V, Ducati C and Ansermet J-Ph 2008 *Nano Lett.* **8** 3683
- [2] Kou X, Fan X, Dumas R K, Lu Q, Zhang Y, Zhu H, Zhang X, Liu K and Xiao J Q 2011 *Adv. Mater.* **23** 1393
- [3] Banerjee A N, Qian S and Joo S W 2011 *Nanotechnology* **22** 035702
- [4] Prina-Mello A, Diao Z and Coey J M D 2006 *J. Nanobiotechnol.* **4** 9
- [5] Kuanr B K, Veerakumar V, Marson R, Mishra S R, Camley R E and Celinski Z 2009 *Appl. Phys. Lett.* **94** 202505
- [6] Tanase M, Felton E J, Gray D S, Hultgren A, Chen C S and Reich D H 2005 *Lab Chip* **5** 598
- [7] Gao N, Wang H J and Yang E H 2010 *Nanotechnology* **21** 105107
- [8] Mehta K K, Wu T-H and Chiou E P Y 2008 *Appl. Phys. Lett.* **93** 254102
- [9] Masuda H and Fukuda K 1995 *Science* **268** 1466
- [10] Lee W, Osele R U and Nielsch K 2006 *Nature Mater.* **5** 741
- [11] Vazquez M and Vivas L G 2011 *Phys. Status Solidi b* **248** 2368
- [12] Schlörb H, Haehnel V, Khatri M S, Srivastav A, Kumar A, Schultz L and Fahler S 2010 *Phys. Status Solidi b* **247** 2364
- [13] Ebels U, Radulescu A, Henry Y, Piroux L and Ounadjela K 2000 *Phys. Rev. Lett.* **84** 983
- [14] Ivanov Yu P, Vivas L G, Asenjo A, Chuvilin A, Chubykalo-Fesenko O and Vázquez M 2013 *Europhys. Lett.* **102** 17009
- [15] Wang T, Wang Y, Fu Y, Hasegawa T, Li F S, Saito H and Ishio S 2009 *Nanotechnology* **20** 105707
- [16] Liu Z, Chang P-C, Chang C-C, Galaktionov E, Bergmann G and Lu J G 2008 *Adv. Funct. Mater.* **18** 1573
- [17] Pan H, Liu B, Poh J Y, Ch, Lim S, Ding J, Feng Y, Huan C H A and Lin J 2005 *J. Phys. Chem. B* **109** 3094
- [18] Henry Y, Ounadjela K, Piroux L, Dubois S, George J-M and Duval J-L 2001 *Eur. Phys. J. B* **20** 35



- [19] Ye Z, Liu H, Luo Z, Lee H-G, Wu W, Naugle D G and Lyuksyutov I 2009 *Nanotechnology* **20** 045704
- [20] Brown W F 1963 *Phys. Rev.* **130** 1677
- [21] Aharoni A 1997 *J. Appl. Phys.* **82** 1281
- [22] Escrig J, Lavin R, Palma J L, Denardin J C, Altbir D, Cortes A and Gomez H 2008 *Nanotechnology* **19** 075713
- [23] Hertel R and Kirschner J 2004 *Physica B* **343** 206
- [24] Vivas L G, Escrig J, Trabada D G, Badini-Confalonieri G A and Vázquez M 2012 *Appl. Phys. Lett.* **100** 252405
- [25] Vivas L G, Vazquez M, Escrig J, Allende S, Altbir D, Leitao D C and Araujo J P 2012 *Phys. Rev. B* **85** 035439
- [26] Skomski R, Zeng H and Sellmyer D J 2002 *J. Magn. Magn. Mater.* **249** 175
- [27] Vila L, Darques M, Encinas A, Ebels U, George J-M, Faini G, Thiaville A and Piraux L 2009 *Phys. Rev. B* **79** 172410
- [28] Lebecki K M and Donahue M J 2010 *Phys. Rev. B* **82** 096401
- [29] Lee J, Suess D, Schrefl T, Oh K H and Fidler J 2007 *J. Magn. Magn. Mater.* **310** 2445
- [30] Hertel R 2002 *J. Magn. Magn. Mater.* **249** 251
- [31] Forster H *et al* 2002 *IEEE Trans. Magn.* **38** 2580
- [32] Stoleriu L, Pinzaru C and Stancu A 2012 *Appl. Phys. Lett.* **100** 122404
- [33] Vivas L G, Ivanov Yu P, Trabada D G, Proenca M P, Chubykalo-Fesenko O and Vázquez M 2013 *Nanotechnology* **24** 105703
- [34] Bran C, Ivanov Yu P, Trabada D G, Tomkowicz J, del Real R P, Chubykalo-Fesenko O and Vazquez M 2013 *IEEE Trans. Magn.* **49** 4491
- [35] Han X, Liu Q, Wang J, Li S, Ren Y, Liu R and Li F 2009 *J. Phys. D: Appl. Phys.* **42** 095005
- [36] Ferre R, Ounadjela K, George J M, Piraux L and Dubois S 1997 *Phys. Rev. B* **56** 14066
- [37] Ren Y, Wang J, Liu Q, Dai Y, Zhang B and Yan L 2011 *J. Mater. Sci.* **46** 7545
- [38] Scholz W, Fidler J, Schrefl T, Suess D, Dittrich R, Forster H and Tsiantos V 2003 *Comput. Mater. Sci.* **28** 366
- [39] Liu Y, Sellmyer D J and Shindo D (ed) 2005 *Handbook of Advanced Magnetic Materials: Nanostructural Effects* vol 1 (Berlin: Springer)
- [40] Jamet M, Dupuis V, Mélinon P, Guiraud G and Pérez A 2000 *Phys. Rev. B* **62** 493
- [41] Fisher J E 1970 *Thin Solid Films* **5** 53
- [42] Cullity B D 1972 *Introduction to Magnetic Materials* (Reading, MA: Addison-Wesley)
- [43] Bran C, Ivanov Yu P, Garcia J, del Real R P, Prida V M, Chubykalo-Fesenko O and Vazquez M 2013 *J. Appl. Phys.* **114** 043908
- [44] Salem M S, Sergelius P, Zierold R, Montero Moreno J M, Gorlitz D and Nielsch K 2012 *J. Mater. Chem.* **22** 8549
- [45] Navas D, Asenjo A, Jaafar M, Pirota K R, Hernández-Vélez M, Sanz R, Lee W, Nielsch K, Batallán F and Vázquez M 2005 *J. Magn. Magn. Mater.* **290–291** 191
- [46] Zheng M, Menon L, Zeng H, Liu Y, Bandyopadhyay S, Kirby R D and Sellmyer D J 2000 *Phys. Rev. B* **62** 12282
- [47] Nielsch K, Wehrspohn R B, Barthel J, Kirschner J, Fischer S F, Kronmüller H, Schweinböck T, Weiss D and Gosele U 2002 *J. Magn. Magn. Mater.* **249** 234
- [48] Fert A and Piraux L 1999 *J. Magn. Magn. Mater.* **200** 338
- [49] Nielsch K, Wehrspohn R B, Barthel J, Kirschner J, Gosele U, Fischer S F and Kronmüller H 2001 *Appl. Phys. Lett.* **79** 1360
- [50] Escrig J, Altbir D, Jaafar M, Navas D, Asenjo A and Vazquez M 2007 *Phys. Rev. B* **75** 184429
- [51] Thongmee S, Pang H L, Yi J B, Ding J, Lin J Y and Van L H 2009 *Acta Mater.* **57** 2482
- [52] Haehnel V, Fahler S, Schaaf P, Miglierini M, Mickel C, Schultz L and Schlorb H 2010 *Acta Mater.* **58** 2330
- [53] Sellmyer J, Zheng M and Skomski R 2001 *J. Phys.: Condens. Matter.* **13** R433
- [54] Menon L, Zheng M, Zeng H, Bandyopadhyay S and Sellmyer D J 2000 *J. Electron. Mater.* **29** 510
- [55] Wang J B, Zhou X Z, Liu Q F, Xue D S, Li F S, Li B, Kunkel H P and Williams G 2004 *Nanotechnology* **15** 485
- [56] Yang S G, Zhu H, Yu D L, Jin Z Q, Tang S L and Du Y W 2000 *J. Magn. Magn. Mater.* **222** 97
- [57] Paulus P M, Luis F, Kroll M, Schmid G and de Jongh L J 2001 *J. Magn. Magn. Mater.* **224** 180
- [58] Zhang J, Jones G A, Shen T H, Donnelly S E and Li G H 2007 *J. Appl. Phys.* **101** 054310
- [59] Yang S G, Zhu H, Ni G, Yu D L, Tang S L and Du Y W 2000 *J. Phys. D: Appl. Phys.* **33** 2388
- [60] Kazadi M B A, Rivas J, Zaragoza G, Lopez-Quintela M A and Blanco M C 2001 *J. Appl. Phys.* **89** 3393
- [61] Rivas J, Kazadi M B A, Zaragoza G, Blanco M C and Lopez-Quintela M A 2002 *J. Magn. Magn. Mater.* **249** 220
- [62] Pirota K R, Beron F, Zanchet D, Rocha T C R, Navas D, Torrejon J, Vazquez M and Knobel M 2011 *J. Appl. Phys.* **109** 083919
- [63] Vivas L G, Yanes R, Chubykalo-Fesenko O and Vazquez M 2011 *Appl. Phys. Lett.* **98** 232507
- [64] Cattaneo L, Franz S, Albertini F, Ranzieri P, Vincenzo A, Bestetti M and Cavallotti P L 2012 *Electrochim. Acta* **85** 57
- [65] Ren Y, Liu Q F, Li S L, Wang J B and Han X H 2009 *J. Magn. Magn. Mater.* **321** 226
- [66] Ramazani A, Kashi M A and Seyedi G 2012 *J. Magn. Magn. Mater.* **324** 1826
- [67] Qin D H, Peng Y, Cao L and Li H L 2003 *Chem. Phys. Lett.* **374** 661
- [68] Wang R L, Tang S L, Shi Y G, Fei X L, Nie B and Du Y W 2008 *J. Appl. Phys.* **103** 07D507
- [69] Ramazanin A, Almasi Kashi M, Kabiri S and Zanguri M 2011 *J. Cryst. Growth* **327** 78
- [70] Cao L, Qiu X, Ding J, Li H and Chen L 2006 *J. Mater. Sci.* **41** 2211
- [71] Stoner E C and Wohlfarth E P 1948 *Philos. Trans. R. Soc. A* **240** 599
- [72] Ivanov Yu P, Trabada D G, Chubykalo-Fesenko O and Vázquez M, to be published
- [73] Park J J, Reddy M, Mudivarthi C, Downey P R, Stadler B J H and Flatau A B 2010 *J. Appl. Phys.* **107** 09A954